JMR Abstracts

Acting Editor-in-Chief: Robert P. Frankenthal • Associate Editors: Shigeyuki Sômiya, Heinrich J. Wollenberger

Abstracts for June 1999 Journal of Materials Research *Volume 14, Number 6*

TABLE OF CONTENTS

SPECIAL SECTION: NANOINDENTATION

RAPID COMMUNICATIONS

ARTICLES

X-ray diffraction and microstructural studies in 2 : 17 type Sm–Co magnetic alloys containing Fe, Cu, and Zr
R. Gopalan, T.S.R.K. Sastry, A.K. Singh, V. Chandrasekaran

Kinetics and mechanism of low-temperature internal oxidation of Ag–2 and 4 at.% Mg alloys
M.O. Rikel, W. Goldacker

Scanning acoustic microscopy investigation of melted collagen in thermoplastic leather
A. Wyler, G. Golan

Mutually reactive elements in a glass host matrix: Ag and S ion implantation in silica
R. Bertoncello, S. Gross, F. Trivillin, E. Cattaruzza, G. Mattei, F. Caccavale, P. Mazzoldi, G. Battaglin, S. Daolio

Preparation of Ti-less aliovalent substituted isomorphs of $KTiOPO_4$
V.I. Chani, K. Shimamura, S. Endo, T. Fukuda

Atomic force microscopic studies of oxide thin films on organic self-assembled monolayers
T.P. Niesen, M.R. De Guire, J. Bill, F. Aldinger, M. Rühle, A. Fischer, F.C. Jentoft, R. Schlögl

Preparation and ferroelectric properties of mixed composition layered lead zirconate titanate thin films for nonvolatile memory applications
S-H. Kim, O-J. Kim, S.K. Streiffer, and A.I. Kingon

Dielectric properties of $Ln(Mg_{1/2}Ti_{1/2})O_3$ as substrates for high-Tc superconductor thin films
S-Y. Cho, C-H. Kim, D-W. Kim, K.S. Hong, J-H. Kim

Possible evidence for the stabilization of β-carbon nitride by high-energy ball milling
Y. Fahmy, T.D. Shen, D.A. Tucker, R.L. Spontak, C.C. Koch

Deposition, structure, and hardness of polycrystalline transition-metal nitride superlattice films
X. Chu, M.S. Wong, W.D. Sproul, S.A. Barnett

Plastic deformation in impure nanocrystalline ceramics
R. Chaim

Reactivity in the chromium oxide–calcium fluoride system: An empirical approach
F. Vos, L. Delaey, M. De Bonte, L. Froyen

Mechanism of in-plane texture development by ion-beam-assisted deposition
H. Ji, G.S. Was

Magnetoresistance, temporal evolution, and relaxation of the electrical resistivity in the re-entrant semiconducting $La_{0.80}Ba_{0.20}CoO_3$ perovskite
R.D. Sánchez, J. Mira, J. Rivas, M.P. Breijo, M.A. Señarís-Rodríguez

Spark plasma sintering of a Nd–Fe–B magnetic alloy
Z.G. Liu, M. Umemoto, S. Hirosawa, H. Kanekiyo

Grain boundary grooving by surface diffusion in $SrTiO_3$ bicrystal
M. Jin. E. Shimada, Y. Ikuma

Substrate temperature: A critical parameter for the growth of microcrystalline silicon-carbon alloy thin films at low power
A. Dasgupta, S.C. Saha, S. Ray, R. Carius

Isothermal sections in the Cr–Ga–N system in the 650–1000 °C temperature range
L. Farber, M.W. Barsoum

An investigation of carbon nanotubes obtained from the decomposition of methane over reduced $Mg_{1-x}M_xAl_2O_4$ spinel catalysts
A. Govindaraj, E. Flahaut, Ch. Laurent, A. Peigney, A. Rousset, C.N.R. Rao

Microstructural studies by transmission electron microscopy of the formation of ultrathin PtSi layers with novel silicidation processes
S. Jin, H. Bender, R.A. Donaton, K. Maex

Orientation relationship and interfaces in nonfaceted-nonfaceted $ZrO_2(c)$–$CaZrO_3$ lamellar eutectics
A. Larrea, V.M. Orera, J.I. Peña, R.I. Merino

A dense transparent ink-jet receptive film that provides instantaneous print drying
B.E. Yoldas

Formation and phase transition of VO_2 precipitates embedded in sapphire
L.A. Gea, J.D. Budai, L.A. Boatner

Preparation of non-aggregated Y_2O_3 : Eu phosphor particles by a spray pyrolysis method
Y.C. Kang, S.B. Park, I.W. Lenggoro, K. Okuyama

Crystal defects of mordenite structures
S.G. Song

The decisive role of oxide content in the formation and crystallization of gallium-lanthanum-sulphide glass
R. Li, D. Furniss, H. Bagshaw, A.B. Seddon

Oxygen and phosphorus coordination around iron in crystalline ferric ferrous pyrophosphate and iron-phosphate glasses with UO_2 or Na_2O
C.H. Booth, P.G. Allen, J.J. Bucher, N.M. Edelstein, D.K. Shuh, G.K. Marasinghe, M. Karabulut, C.S. Ray, D.E. Day

Synthesis and optical characterization of stable and highly luminescent poly-(9-vinylcarbazole)–aluminum-tris-(8-hydroxyquinoline) blends
M. Allegrini, A. Arena, R. Girlanda, C. Pace, S. Patanè, G. Saitta

New insights on the crystalline forms in binary systems of n-alkanes: Characterization of the solid ordered phases in the phase diagram tricosane + pentacosane
F. Rajabalee, V. Metivaud, D. Mondieig, Y. Haget, M.A. Cuevas-Diarte

Hydrothermal growth of hydroxyapatite single crystals under natural convection
K. Teraoka, A. Ito, K. Onuma, T. Tateishi, S. Tsutsumi

***c*-axis lithium niobate thin film growth on silicon using solid-source metalorganic chemical vapor deposition**
S.Y. Lee, R.S. Feigelson

***In situ* surface modification and growth of ultra-smooth amorphous carbon films by direct carbon ion-beam deposition**
M.H. Sohn, S.I. Kim

Microstructural investigation of iron nitride layers formed by low-temperature gaseous nitriding
D.K. Inia, A.M. Vredenberg, D.O. Boerma, F.D. Tichelaar, H. Schut, A. van Veen

Hydraulic activity and microstructural characterization of new fly ash-belite cements synthesized at different temperatures
A. Guerrero, S. Goñi, A. Macías, M.P. Luxán

ABSTRACTS

SPECIAL SECTION: NANOINDENTATION

Indentation plastic displacement field: Part I. The case of soft films on hard substrates

T.Y. Tsui,[1] J. Vlassak,[2] W.D. Nix[2]
([1]Advanced Micro Devices, [2]Stanford University)

The plastic deformation behavior of Knoop indentations made in a soft, porous titanium/aluminum multilayered thin film on a hard silicon substrate is studied through use of the focused-ion-beam milling and imaging technique. Pileup is observed for indentations with depths larger than 30% of the total film thickness. Analysis of the indentation cross sections shows that plastic deformation around the indentation is partly accommodated by the closing of the pores within the multilayers. This densification process reduces the amount of pileup formed below what is predicted by finite element simulations. Experimental results show that the pileup is formed by an increase of the titanium layer thicknesses near the edges of the indentation. The thickness increase is largest near the film/substrate interface and decreases toward the surface of the multilayered film. The amount of normal compression near the center of the indenter is characterized, and it is demonstrated that the deformation becomes more nonuniform with increasing indentation depth.

Order No.: JA906-001

Indentation plastic displacement field: Part II. The case of hard films on soft substrates

T.Y. Tsui,[1] J. Vlassak,[2] W.D. Nix[2]
([1]Advanced Micro Devices, [2]Stanford University)

The plastic displacements around Knoop indentations made in hard titanium/aluminum multilayered films on soft aluminum alloy substrates have been studied. Indentations were cross-sectioned and imaged using the focused-ion-beam (FIB) milling techniques and high-resolution scanning electron microscopy, respectively. The FIB milling method has the advantage of removing material in a localized region without producing mechanical damage to the specimen. The micrographs of the cross-sectioned indentations indicate that most of the plastic deformation around the indentation is dominated by the soft aluminum substrate. There is a very small change in the multilayered film thickness around the indentation, less than 10%. The plastic deformation of the thin film resembles a membrane being deflected by a localized pressure gradient across the membrane. Stress-induced voids are also observed in the multilayered film, especially in the area around the indentation apex. The density and the size of the voids increase with indentation depth. Indentation sink-in effects are also observed in all of the indentations inspected. The experimental results show that the amount of sink-in of the hard film/soft substrate composite is larger than the bulk substrate and film alone. This is confirmed by the finite element analyses conducted in this work.

Order No.: JA906-002

Hard protective overlayers on viscoelastic-plastic substrates

W.W. Gerberich, A. Strojny, K. Yoder, L-S. Cheng
(University of Minnesota)

A simple superposition solution for a point-loaded elastic plate on a soft substrate is proposed. The solution considers a "drumhead" being elastically bent into a compliant substrate that is viscoelastic-plastic. With simplifying assumptions it is found that the drumhead and substrate support loads proportional to $\delta^{1/2}$ and $\delta^{3/2}$, respectively, where δ is the vertical point displacement. At fixed displacement, relaxation proceeds at high loads, but if sufficiently unloaded, recovery or increased load results with time. Qualitative verification of the time-dependent drumhead solution is shown by relaxation and recovery data on polycarbonate covered by polysiloxane, composite or diamondlike carbon coatings, and films.

Order No.: JA906-003

Initial stages of yield in nanoindentation

J.D. Kiely,[1] K.F. Jarausch,[2] J.E. Houston,[1] P.E. Russell[2]
([1]Sandia National Laboratories, [2]North Carolina State University)

We have used the interfacial force microscope to perform nanoindentations on Au single-crystal surfaces. We have observed two distinct regimes of plastic deformation, which are distinguished by the magnitude of discontinuities in load relaxation. At lower stresses, relaxation occurs in small deviations from elastic behavior, while at the higher stresses they take the form of large load drops, often resulting in complete relaxation of the applied load. These major events create a relatively wide plastic zone that subsequently deepens more rapidly than it widens. We discuss these findings in terms of contrasting models of dislocation processes in the two regimes.

Order No.: JA906-004

Nanoindentation of a 10-nm-thick thin film

T. Sawa, Y. Akiyama, A. Shimamoto, K. Tanaka
(Nagaoka University of Technology)

In a nanometer order nanoindentation test, roundness or truncation of the indenter tip cannot be avoided. In this paper, we have analyzed the indentation problem of a rounded triangular indentation into a layered elastic half-space by a finite element analysis and then established a method to estimate the intrinsic elastic modulus of the film from the nanoindentation data. The method was applied to analyze the nanoindentation data of less-than-10 nm penetration depth on a 10-nm-thick diamondlike carbon film deposited on a 50-nm-thick magnetic layer.

Order No.: JA906-005

Nanoindentation and incipient plasticity

E.B. Tadmor,[1] R. Miller,[1] R. Phillips,[1] M. Ortiz[2]
([1]Brown University, [2]California Institute of Technology)

This paper presents a large-scale atomic resolution simulation of nanoindentation into a thin aluminum film using the recently introduced quasicontinuum method. The purpose of the simulation was to study the initial stages of plastic deformation under the action of an indenter. Two different crystallographic orientations of the film and two different indenter geometries (a rectangular prism and a cylinder) were studied. We obtained both macroscopic load versus indentation depth curves, as well as microscopic quantities, such as the Peierls stress and density of geometrically necessary dislocations beneath the indenter. In addition, we obtain detailed information regarding the atomistic mechanisms responsible for the macroscopic curves. A strong dependence on geometry and orientation is observed. Two different microscopic mechanisms are observed to accommodate the applied loading: (i) nucleation and subsequent propagation into the bulk of edge dislocation dipoles and (ii) deformation twinning.

Order No.: JA906-006

A study of the submicron intent-induced plastic deformation

C.F. Robertson,[1] M.C. Fivel[2]
([1]DTA/SRMP, [2]CNRS-INPG)

A new method has been developed to achieve a better understanding of submicron indent-induced plastic deformation. This method combines numerical modeling and various experimental data and techniques. Three-dimensional discrete dislocation dynamics simulation and finite element method were used to model the experimental conditions associated with nanoindentation testing in fcc crystals. Transmission electron microscopy observations of the indent-induced plastic volume and analysis of the experimental loading curve help in defining a complete set of dislocation nucleation rules, including the shape of the nucleated loops and the corresponding macroscopic loading. A validation of the model is performed through direct comparisons between a simulation and experiments for a nanoindentation test on a [001] copper single crystal up to 50 nm deep.

Order No.: JA906-007

Deconvolution of hardness from data obtained from nanoindentation of rough surfaces

M.S. Bobji, S.K. Biswas
(Indian Institute of Science)

Variation of hardness with penetration in nanoindentation of a rough surface is a compound effect of variation in asperity geometry with penetration, designated geometric effect, and genuine property gradients with depth as may exist in a near-surface zone. We simulate indentation of a rough surface numerically to elucidate the geometric effects and validate it by some model "macro" experiments. Finally, we formulate a general framework to deconvolute genuine property variation by normalizing the measured hardness with the geometric effect.

Order No.: JA906-008

Energy considerations regarding yield points during indentation

D.F. Bahr,[1] D.E. Wilson,[1] D.A. Crowson[2]
([1]Washington State University, [2]Nanomechanics Research Laboratory)

Two experiments that probe the nature of the rapid transition from elastic to plastic deformation are described. The load, and therefore stress, at which this yield point occurs are shown to be relatively independent of temperature in an iron alloy. When stresses lower than those required to generate a yield point during loading are applied for times between seconds and minutes, yielding occurs while the sample is under an applied stress. The time to generate a yield point increases as the applied stress is decreased. The possibilities of dislocation glide loop nucleation, double kink nucleation, and dislocation breakaway from pinning points are examined. Only glide loop nucleation appears to match the experimental observations. Criteria based on the stress-volume requirements of glide loop nucleation and the stress field underneath an indenter are presented which quantitatively describe the experimental data.

Order No.: JA906-009

Compensating for elastic deformation of the indenter in hardness tests of very hard materials

R.Y. Lo, D.B. Bogy
(University of California)

The current method of analysis for hardness measurements by indentation is examined. Although the method is based on Sneddon's solution for an elastic stress field within a homogeneous half-space indented by an elastically deformable indenter, it implicitly assumes a fixed indenter geometry. Therefore, if indentations are made on materials whose hardness or elastic modulus are close to those of the indenter, this method underestimates the contact area and thus, overestimates the hardness and modulus values of the indented materials. A new method, based on the Hertz contact theory, is proposed that accounts for the indenter's elastic deformation and provides a simple way to calculate the tip radius. The restrictions of this method are also indicated and discussed. Finally, the hardness and modulus for two recently developed films are measured by this method, and the results are compared with published finite element method results.

Order No.: JA906-010

Using the P–δ^2 analysis to deconvolute the nanoindentation response of hard-coated systems

M.R. McGurk, T.F. Page
(University of Newcastle)

The continuously recording indentation responses of a number of coated systems, mainly thin (<10 μm) hard nitride coatings on stainless steels and a powder metallurgy tool steel, have been explored using nanoindentation with indenter displacements increasing progressively to values greater than the coating thickness. The resultant load-displacement data have been analyzed not only to produce conventional load-displacement (P–δ) plots, but also to examine the relationship between P and δ^2. Recent models have proposed that there should be a linear P–δ^2 relationship for homogeneous systems and that such plots have the potential to reveal the load/displacement regimes in which either the coating or the substrate, or both, are dominant in controlling the overall behavior of the coated system. By utilizing point-to-point differentiation of the P–δ^2 relationship, this paper extends this approach to confirm not only that these different regimes of behavior may be readily experimentally identified in this way, but also that further details, such as the propagation of cracks, may be recognized. Our analysis also provides a valuable experimental link to models describing the near-surface deformation behavior of coated systems.

Order No.: JA906-011

A critical examination of the fundamental relations used in the analysis of nanoindentation data

J.C. Hay,[1] A. Bolshakov,[2] G.M. Pharr[3,4]
([1]T.J. Watson Research Center, [2]Baker Hughes Inteq,
[3]The University of Tennessee, [4]Oak Ridge National Laboratory)

Methods for analyzing nanoindentation load-displacement data to determine hardness and elastic modulus are based on analytical solutions for the indentation of an elastic half-space by rigid axisymmetric indenters. Careful examination of Sneddon's solution for indentation by a rigid cone reveals several largely ignored features that have important implications for nanoindentation property measurement. Finite element and analytical results are presented that show corrections to Sneddon's equations are needed if accurate results are to be obtained. Without the corrections, the equations underestimate the load and contact stiffness in a manner that leads to errors in the measured hardness and modulus, with the magnitudes of the errors depending on the angle of the indenter and Poisson's ratio of the half-space. First order corrections are derived, and general implications for the interpretation of nanoindentation data are discussed.

Order No.: JA906-012

Substrate composition effects on the interfacial fracture of tantalum nitride films

N.R. Moody,[1] A. Strojny,[2] D.L. Medlin,[1] A. Talin,[3] W.W. Gerberich[2]
([1]Sandia National Laboratories, [2]University of Minnesota, [3]Motorola)

In this study we combined nanoscratch testing with a multilayer sapphire and aluminum nitride single-substrate system to determine the effects of interface composition and structure on susceptibility to fracture of hard, thin tantalum nitride films. Nanoindentation tests showed that the elastic moduli of the tantalum nitride and aluminum nitride films, as well as the sapphire substrate, were essentially equal at 400 GPa. On both portions of the substrate, these tests also showed that near surface hardness was near 35 GPa. Nanoscratch tests triggered long blisters and circular spalls on both the sapphire and aluminum nitride portions of the substrate. The blisters showed that the tantalum nitride film was subjected to a compressive residual stress of –6.7 GPa. The spalls showed that failure occurred along the tantalum nitride film-substrate interface regardless of substrate composition. Most importantly, the blisters and spalls showed that the mode I component of the fracture energies was essentially equal on both substrate materials at a value near 3.1 J/m^2. These energies are on the order of the energies for metallic bonding.

Order No.: JA906-013

Accurate determination of the mechanical properties of thin aluminum films deposited on sapphire flats using nanoindentations

Y.Y. Lim,[1] M.M. Chaudhri,[1] Y. Enomoto[2]
([1]University of Cambridge, [2]Mechanical Engineering Laboratory)

Nanoindentations using a Berkovich diamond indenter have been made on 1-, 2-, and 5-μm-thick 99.99% pure polycrystalline aluminium films thermally evaporated in vacuum onto 2-mm-thick R-cut polished sapphire flats. The projected contact areas of the residual indentations were estimated from the unloading load-displacement curves, and some of the indentations were imaged with an atomic force microscope (AFM). It was found that a large majority of indents showed material pileup, and the projected areas of these indents, as measured with the AFM, were up to 50% greater than those calculated from the unloading curves. This discrepancy between the calculated and directly measured indentation areas has a strong influence on the derived values of Young's modulus and hardness of the aluminium films. Using a new analytical model, Young's modulus of the aluminium films has been determined to be in the range of 50–70 GPa, independent of the relative indentation depth. The composite nanohardness of the 1 and 2 μm thick films was found to have a load-independent value of 1 GPa, whereas the composite nanohardness of the 5-μm film decreased from 1 to 0.7 GPa with increasing indenter penetration. Finally, it has been suggested that, in order to improve the accuracy with which the mechanical properties of thin films or bulk specimens can be determined by nanoindentation techniques, the projected contact areas should be measured by direct methods, such as atomic force microscopy.

Order No.: JA906-014

Micro/nanomechanical and tribological characterization of ultrathin amorphous carbon coatings

X. Li, B. Bhushan
(The Ohio State University)

Micro/nanomechanical and tribological characterization of ultrathin amorphous carbon coatings, deposited by filtered cathodic arc (FCA), direct ion beam (IB), electron-cyclotron resonance plasma chemical vapor deposition (ECR-CVD), and sputter (SP) deposition processes on Si substrate have been conducted using a nanoindenter with a nanoscratch attachment and an accelerated ball-on-flat tribometer. Coating thicknesses of 20, 10, 5 nm and, for the first time, 3.5 nm have been investigated. It was found the FCA coating exhibits the highest hardness and elastic modulus, followed by the ECR-CVD, IB, and SP coatings. In general, the thicker coatings exhibited better scratch/wear performance than the thinner coatings due to their better load carrying capacity as compared to the thinner coatings. At 20 nm, the FCA and ECR-CVD coatings showed the best scratch and wear resistance, while the IB and ECR-CVD coatings showed the best scratch and wear resistance at 10 nm. Five-nanometer-thick coatings showed reasonable scratch and wear resistance, while 3.5 nm thick coatings showed extremely low load-carrying capacity and poor scratch and wear resistance. It appears that the 3.5-nm coatings studied are infeasible for scratch and wear resistance applications as of now.

Order No.: JA906-015

Ultra-micro-indentation of silicon and compound semiconductors with spherical indenters

J.S. Williams,[1] Y. Chen,[1] J. Wong-Leung,[1] A. Kerr,[1] M.V. Swain[2]
([1]Australian National University,
[2]CSIRO Division of Telecommunications and Industrial Physics)

Details of microindentation of silicon, such as the semiconductor-to-metal transformation, which takes place on loading, have been examined using spherical indenters. Various forms of silicon were studied, including heavily boron-doped wafers and silicon damaged and amorphized by ion implantation as well as material containing dislocations. Results indicate that only silicon, which contains high concentrations of point defects or is amorphous, exhibits mechanical properties that differ significantly from undoped, defect-free crystal. Amorphous silicon exhibits plastic flow under low indentation pressures and does not appear to undergo phase transformations on loading and unloading. Indentation of compound semiconductors is also studied and the load and unload behavior at room temperature is quite different from that of silicon. Both gallium arsenide and indium phosphide, for example, undergo slip-induced plasticity above a critical load.

Order No.: JA906-016

Nanoindentation of particulate coatings

M.J. Adams, A. Akram, B.J. Briscoe, D. Parsonage
(Imperial College of Science, Technology and Medicine)

A knowledge of the formation and rupture mechanisms for agglomerates is essential when seeking to model equipment designed to produce and process such materials. In the work described here, nanoindentation of "two-dimensional" agglomerate films, basically particulate coatings, was carried out to establish a means of identifying the generic breakage mechanisms for agglomerates. Selected applied load and penetration depth data in the range (0.02 mN and 700 nm, respectively) are provided as a function of the loading time during continuous loading for a model system composed rather of monodispersed colloidal silica particles (20–24 nm diameter) bound with a poly(methyl methacrylate) at 5 vol%. It is argued that these data enable the sequence of binder bridge failures to be observed, thus giving an indication of the breakage mechanism of the agglomerate and also the strength of the individual junctions. These data are also incorporated into a mechanical model that describes the rupture and deformation behavior of these planar agglomerate systems.

Order No.: JA906-017

RAPID COMMUNICATIONS

Subsolidus phase equilibria in the La_2O_3–Ga_2O_3–NiO system

M. Hrovat, S. Bernik, J. Holc, Z. Samardžija
(Jožef Stefan Institute)

Subsolidus equilibria in air in the La_2O_3–Ga_2O_3–NiO system were studied with the aim of obtaining information on possible interactions between a $LaGaO_3$-based solid electrolyte and NiO during preparation of the anode in solid oxide fuel cells. No ternary compound was found. The tie lines are between $La_4Ga_2O_7$–La_2NiO_4, $LaGaO_3$–La_2NiO_4, $LaGaO_3$–NiO, and $LaGaO_3$–$NiGa_2O_4$.

Order No.: JA906-018

The effect of target crystallography on the growth of $Pb(Mg_{1/3}Nb_{2/3})O_3$ thin films using pulsed laser deposition

M.H. Corbett, G. Catalan, R.M. Bowman, J.M. Gregg
(The Queen's University of Belfast)

Pulsed laser deposition has been used to make two sets of lead magnesium niobate thin films grown on single-crystal {100} MgO substrates. One set was fabricated using a perovskite-rich target while the other used a pyrochlore-rich target. It was found that the growth conditions required to produce almost 100% perovskite $Pb(Mg_{1/3}Nb_{2/3})O_3$ (PMN) films were largely independent of target crystallography. Films were characterized crystallographically using x-ray diffraction and plan view transmission electron microscopy, chemically using energy dispersive x-ray analysis, and electrically by fabricating a planar thin film capacitor structure and monitoring capacitance as a function of temperature. All characterization techniques indicated that perovskite PMN thin films had been successfully fabricated.

Order No.: JA906-019

Evidence for continuous areas of crystalline β–C_3N_4 in sputter-deposited thin films

A.K.M.S. Chowdhury,[1] D.C. Cameron,[1] M.S.J. Hashmi,[1] J.M. Gregg[2]
([1]Dublin City University, [2]The Queen's University of Belfast)

Carbon nitride films have been deposited using Penning-type opposed target dc reactive sputtering. These films show large (>10 μm^2) continuous areas of nanocrystalline material in an amorphous matrix. Electron diffraction shows the nanocrystalline areas to have crystallography consistent with the β–C_3N_4 phase. Film chemistry analysis using Rutherford backscattering and Raman spectroscopy indicates that only carbon, nitrogen, and trace levels of hydrogen are present. Given this film chemistry and the fit of diffraction data to that predicted for the β–C_3N_4 structure, it seems likely that the sputtering parameters used have, indeed, produced continuous regions of the elusive β–C_3N_4 phase.

Order No.: JA906-020

Measuring the critical thickness of thin metalorganic precursor films

R.K. Roeder, E.B. Slamovich
(Purdue University)

Successful application of sol-gel, metalorganic decomposition, or hydrothermal routes to ceramic thin films depends on the mechanical integrity of the precursor film. Above a critical thickness, a precursor film will crack or decohere from the substrate during drying. The cracking and thickness of thin metalorganic precursor films were simultaneously observed during drying using a standard optical microscope. Isochromatic color fringes produced by interference of reflected white light were used to monitor film thickness. The critical film thickness was determined by the color fringe corresponding to the thickness at which propagating cracks terminated. As a demonstration of the technique, the critical thickness of titanium di(isopropoxide) bis(ethyl acetoacetate) films was measured, showing increased critical thickness with the addition of small amounts of an elastomeric polymer.

Order No.: JA906-021

Lower crystallization temperature of sol-gel $PbTiO_3$ on Ti/Pt-coated substrates

R.E. Avila,[1] T.P. Velilla,[2] P.J. Retuert[2]
([1]Comisión Chilena de Energía Nuclear, [2]Universidad de Chile)

$PbTiO_3$ (PT) thin films have been deposited by sol-gel on Pt/Si, SiO_2/Si, Pt/Ti/SiO_2/Si, and Ti/Pt/Ti/SiO_2/Si and annealed for 45 min in the 400–670 °C range. Analysis by x-ray diffraction and spectroscopic ellipsometry shows that the Ti overlayer promotes early crystallization in the tetragonal pervoskite phase, reducing the presence of a second phase, tentatively identified as pyro-chlore, starting at 450 °C. The refractive index and extinction coefficient (n, k) of the PT film increase rapidly with the sintering temperature in the range 450–570 °C and saturate by 570 °C to values of n varying from 2.4 to 2.9, and k from 0.03 to 0.3, over the 1.65–2.95 eV range. Most of the increase of n is related to thin film densification.

Order No.: JA906-022

A new method to study cyclic deformation of thin films in tension and compression

M. Hommel, O. Kraft, E. Arzt
(Max-Planck-Institut für Metallforschung)

In this paper, a new method to study cyclic plastic deformation in thin metal films is presented. Cu films were deposited onto compliant substrates allowing the film to be subjected to tensile and compressive stresses on loading and unloading of the film/substrate composite. The film stress was measured *in situ* by x-ray diffraction. First results lend to characteristic stress-strain hysteresis curves, indicative of fatigue processes in small dimensions.

Order No.: JA906-023

Effect of surface kinetics on the step coverage during chemical vapor deposition

G.S. Hwang,[1] S.H. Moon,[1] S.W. Nam,[2] C.B. Shin[3]
([1]Seoul National University, [2]Korea Institute of Science and Technology, [3]Ajou University)

Profile evolution simulations during chemical vapor deposition based on a 2D continuum model reveal that the type of surface kinetics plays an important role in determining step coverage of films deposited in high aspect ratio trenches and vias. Linear surface kinetics, resulting from an adsorption rate limited process, is found to cause difficulty in bringing about conformal step coverage in deep

narrow trenches without reducing the growth rate considerably. Under such condition, void-free filling cannot be achieved while maintaining a growth rate acceptable to integrated circuit manufacturing. The numerical study also suggests that the high tendency of the precursor for chemical equilibrium on a surface, resulting in nonlinear kinetics by a surface reaction limited process, is crucial to achieve a uniform step coverage as typically observed in SiO_2 deposition from tetraethylorthosilicate.
Order No.: JA906-024

Synthesis and characteristics of ZnS/CdS composite nanocrystals in block copolymer micelle

D. Wang, Y. Cao, X. Zhang, X. Qian, X. Ai, Z. Liu, F. Liu, D. Wang, Y. Bai, T. Li, X. Tang
(Jilin University)

In hydroxylated poly(styrene-*b*-butadiene-*b*-styrene) micelle, ZnS/CdS composite nanocrystals were prepared by adding Cd^{2+} ions and Zn^{2+} ions to the system sequentially. The resulting composites were identified with elemental analysis, transmission electron microscopy, x-ray diffraction, surface photovoltage spectroscopy, and electric-field-induced surface photovoltage spectroscopy.
Order No.: JA906-025

ARTICLES

Epitaxial cerium oxide buffer layers and $YBa_2Cu_3O_{7-\delta}$ thin films for microwave device applications

S.N. Jacobsen, L.D. Madsen, U. Helmersson
(Linköping University)

CeO_2 films with thicknesses ranging from 8.8 to 199 nm were grown on Al_2O_3 ($1\bar{1}02$) (R-cut) substrates by off-axis rf magnetron sputtering. X-ray diffraction showed an epitaxial relationship with the CeO_2 (001) planes parallel to the Al_2O_3 ($1\bar{1}02$) planes for all film thicknesses. Atomic force microscopy (AFM) revealed a rough surface morphology consisting of crystallites with lateral dimensions of 10–90 nm. In the thinnest film, these crystallites were regularly shaped and uniformly distributed on the substrate, while they were rectangularly shaped and oriented mainly in two directions, orthogonal to each other, in the thicker films. The surface roughness of the films increased with increasing layer thickness. Characterization of the microstructure was done by cross-sectional transmission electron microscopy (XTEM) and showed a polycrystalline, highly oriented, columnar structure with a top layer terminated by (111)-facets. High-quality $YBa_2Cu_3O_{7-\delta}$ (YBCO) thin films were deposited directly onto the CeO_2 layers. XTEM rather surprisingly showed a smooth interface between the YBCO and CeO_2 layer. Postdeposition *ex situ* annealing was carried out on two CeO_2 films and evaluated by AFM. Upon annealing samples at 930 °C, a relatively smooth morphology without facets was obtained. Annealing films at 800 °C caused no appreciable change in surface morphology, whereas igniting a YBCO plasma during a similar anneal clearly altered the sample surface, giving rounded facets.
Order No.: JA906-026

X-ray diffraction study of texture in melt-processed Gd-123 as a function of 211 concentration

E. Sudhakar Reddy, A.K. Singh, T. Rajasekharan
(Defence Metallurgical Research laboratory)

The texture of melt-processed GdBCO superconductor is studied as a function of Gd_2BaCuO_5 additions, using a texture goniometer. A systematic variation observed in the background intensity is connected to the microstructural variations and powder x-ray diffraction spectra.
Order No.: JA906-027

Cross-sectional observation on the indentation of [001] silicon

Y.Q. Wu,[1] G.Y. Shi,[2] Y.B. Xu[1]
([1]The Chinese Academy of Sciences, [2]University of Liaoning)

A transmission electron micrograph of cross-sectionally viewed Vickers indentation made on the surface of (001) silicon at ambient temperature was obtained. The picture clearly reveals a triangle area, pointing downwards and having nondiffraction-contrast, left after unloading, which further confirms the amorphized range induced by indentation in silicon. Analysis of the picture directly manifests a significant recovery of indentation depth. Surface shape and range of the amorphous silicon region do not coincide with that of the indenter and the corresponding distribution pattern of hydrostatic stress beneath indentation predicted by elastoplastic theory, respectively. It seems that the amorphization could not be attributed to the result of hydrostatic stress alone.
Order No.: JA906-028

Effect of doping level during rapid thermal processing of multilayer structures

A.R. Abramson,[1] P. Nieva,[2] H. Tada,[1] P. Zavracky,[2] I.N. Miaoulis,[1] P.Y. Wong[1]
([1]Tufts University, [2]Northeastern University)

A numerical model has been developed to examine the temperature history of a multilayer wafer undergoing rapid thermal processing for various doping densities. Partial transparency and thin film interference effects are considered. Doping levels from ~10^{15} to ~10^{18} cm^{-3} are examined. Numerical temperature predictions of the lightly doped wafer are compared with experimental measurements. Heating rates for the lightly doped wafer fluctuate due to partial transparency effects and reach a maximum of ~50 °C/s. The heavily doped wafer sees a maximum heating rate of ~100 °C/s. Because the wafers are opaque above 700 °C regardless of their level of doping, all wafers reach steadystate at ~845 °C.
Order No.: JA906-029

Synthesis of bulk polycrystalline indium nitride at subatmospheric pressures

J.S. Dyck, K. Kash, C.C. Hayman, A. Argoitia, M.T. Grossner, J.C. Angus, W-L. Zhou
(Case Western Reserve University)

Polycrystalline, wurtzitic indium nitride was synthesized by saturating indium with nitrogen from microwave plasma sources. The structure was confirmed by x-ray diffraction, electron diffraction, and elemental analysis. Two types of growth were observed: (i) dendritic crystals on the original melt surface, and (ii) hexagonal platelets adjacent to the In metal source on the upper edge of the crucible. The method does not involve a foreign substrate to initiate growth and is a potential alternative to the high-pressure techniques normally associated with bulk growth of indium nitride. The lattice parameters were $a = 3.5366 \pm 0.0005$ Å and $c = 5.7009 \pm 0.0005$ Å, with $c/a = 1.612 \pm 0.0005$.
Order No.: JA906-030

Microstructure and 1000–1400 K mechanical properties of cryomilled NiAl–0.7Zr

J.D. Whittenberger,[1] A. Garg,[2] M.G. Hebsur[3]
([1]NASA-Glenn Research Center, [2]AYT Corp. at NASA-Glenn Research Center, [3]OAI/NASA)

An attempt has been made to improve the intermediate temperature strength of cryomilled NiAl by utilizing third element solid solution or precipitation strengthening mechanisms. To this end an NiAl–0.7(at.%) Zr alloy was cryomilled, densified by hot extrusion, and tested between 1000 and 1400 K. Although over 3 wt% nitrogen was introduced by cryomilling, mechanical testing revealed that the cryomilled NiAl–0.7Zr was significantly weaker than the base alloy between 1000 and 1200 K. Chemical and microstructural analyses revealed that, in addition to ~16 vol% AlN, all the Zr had been converted to ZrN. A thermodynamic analysis of cryomilling indicated that the formation of ZrN could have been anticipated since it is a more stable nitride than AlN. While Zr was an unsatisfactory addition in NiAl, thermodynamics also suggest several alloying elements that might lead to good intermediate temperature strength after cryomilling.
Order No.: JA906-031

X-ray diffraction and microstructural studies in 2 : 17 type Sm–Co magnetic alloys containing Fe, Cu, and Zr

R. Gopalan, T.S.R.K. Sastry, A.K. Singh, V. Chandrasekaran
(Defence Metallurgical Research Laboratory)

X-ray diffraction and microstructural studies were carried out on 2 : 17 type Sm–Co alloys containing Fe, Cu, and Zr (13–14 at.% Sm, 57–60 at.% Co, 20–22 at.% Fe, 4 at.% Cu, and 3 at.% Zr) in as-cast and heat-treated conditions. Microstructural studies revealed that the as-cast alloys contain three phases. It was observed that the samples subjected to sintering at 1463 K for 45 min followed by a solution treatment at 1448 K for 1 h resulted in nearly a single-phase, rhombohedral crystal structure (Th_2Zn_{17}-type). Subsequent isothermal aging at 1123 K and ramp-cooling to 673 K resulted in a mixture of Sm_2Co_{17}- and $SmCo_5$-type phases with the former as major phase. It was also found that samples (Sm > 13 at.%) sintered at temperatures >1463 K showed incipient melting and multiphase formation.
Order No.: JA906-032

Kinetics and mechanism of low-temperature internal oxidation of Ag–2 and 4 at.% Mg alloys

M.O. Rikel,[1] W. Goldacker[2]
([1]Russian Academy of Sciences, [2]Forschungszentrum Karlsruhe GMBH)

Gravimetry and x-ray diffraction were used to study the kinetics and mechanism of internal oxidation in air at 300–600 °C of Ag–2 and 4 at.% Mg alloys. All the features typical of the non-Wagnerian behavior in more dilute alloys (the slower initial and faster intermediate kinetics, oxygen release from the samples at the late stages, and stabilization of highly hyper-stoichiometric oxides with O/Mg up to 1.74 ± 0.02) are also observed in these more concentrated alloys. A linear correlation between the lattice parameter of oxidized alloys, magnesium content, and amount of excess oxygen is found and used for analyzing the published data on the lattice parameters in other oxidized Ag–Mg alloys. Such analysis suggests that, at early stages of low-temperature oxidation, O/Mg ratios could be higher than 4 ± 0.8, which is interpreted as evidence that O–Mg interaction at these stages is trapping of mobile O atoms by immobile Mg atoms, so that oxidation of Ag–Mg alloys can be considered as formation and subsequent decomposition of Ag–Mg–O solid solutions, and it is the decomposition stage that significantly affects the oxidation kinetics. Possible impact of these findings on optimization of alloy-sheath composition and microstructure in Bi2223/AgMg superconducting tapes is discussed.

Order No.: JA906-033

Scanning acoustic microscopy investigation of melted collagen in thermoplastic leather

A. Wyler,[1] G. Golan[2]
([1]Jerusalem College of Technology, [2]Open University of Israel)

A scanning acoustic microscope (SAM) has been used to investigate the structure of thermoplastic leather. This material is formed by pressing fibers of leather under high pressure and moderate temperature. The result is a matrix from transformed, melted fibers in which leftover fibers act as reinforcement. Unlike the scanning electron microscope (SEM), the SAM is able to distinguish between completely and incompletely transformed fibers and also to penetrate the material beneath the surface. The results show that the matrix is built as a domain structure. The advantages of the SAM over the SEM for organic materials are indicated.

Order No.: JA906-034

Mutually reactive elements in a glass host matrix: Ag and S ion implantation in silica

R. Bertoncello,[1] S. Gross,[1] F. Trivillin,[1] E. Cattaruzza,[1] G. Mattei,[1]
F. Caccavale,[1] P. Mazzoldi,[1] G. Battaglin,[2] S. Daolio[3]
([1]Università di Padova, [2]Università di Venezia,
[3]Instituto di Polarografia ed Elettrochimica Preparativa –C.N.R.)

Ag, S, Ag + S, and S + Ag single and double ion implantations in silica glass were performed at room temperature. The implantation energies were chosen to get a projected range of 40 nm. The fluences were 2×10^{16} S^+ cm^{-2} and 5×10^{16} Ag^+ cm^{-2}. Silver interacts weakly with the host silica matrix and forms essentially metallic clusters; this weak interaction between Ag and SiO_2 induces formation of silver silicate rather than silver oxide. Double ion implantations of silver and sulphur lead to chemical interaction between the two species that is critically influenced by the implantation sequence. In particular, in the Ag + S sample silver and sulphur atoms react to form crystalline core(Ag)–shell(Ag_2S) nanoclusters.

Order No.: JA906-035

Preparation of Ti-less aliovalent substituted isomorphs of $KTiOPO_4$

V.I. Chani, K. Shimamura, S. Endo, T. Fukuda
(Tohoku University)

$KTiOPO_4$ (KTP) phase formation in stoichiometric mixtures corresponding to chemical formulas of $\{A^+\}[B^{5+}_{1/2}C^{3+}_{1/2}]O(D^{5+})O_4$ (A = K^+; B = Nb^{5+} and Ta^{5+}; C = Al^{3+}, Cr^{3+}, Ga^{3+}, Fe^{3+}, and In^{3+}; and D = P^{5+} and As^{5+}), and $\{A^+\}[B^{5+}_{2/3}C^{2+}_{1/3}]O(D^{5+})O_4$ (C = Mg^{2+} and Zn^{2+}) prepared by solid-state reaction technique is reported. It was found that the mixtures containing Nb^{5+}, Ga^{3+}, Fe^{3+}, and As^{5+} form the longest series of members of the KTP structural family. KTP phase formation was detected by x-ray powder diffraction analysis. Comparison of the lattice parameters measured with those known for the nonsubstituted crystals of the KTP family was carried out. The data obtained were used for the discussion of variations of KTP structural stability on composition.

Order No.: JA906-036

Atomic force microscopy studies of oxide thin films on organic self-assembled monolayers

T.P. Niesen,[1,2] M.R. De Guire,[1,2] J. Bill,[1,2] F. Aldinger,[1,2] M. Rühle,[1]
A. Fischer,[3] F.C. Jentoft,[3] R. Schlögl[3]
([1]Max-Planck-Institut für Metallforschung, [2]Universität Stuttgart,
[3]Fritz-Haber-Institut der Max-Planck-Gesellschaft)

The surface morphology of TiO_2- and ZrO_2-based thin films deposited from aqueous solution at 70–80 °C onto functionalized organic self-assembled monolayers (SAMs) on silicon has been examined using atomic force microscopy. The films have been previously shown to consist respectively of nanocrystalline TiO_2 (anatase) and nanocrystalline tetragonal ZrO_2 with amorphous basic zirconium sulfate. The films exhibit characteristic surface roughnesses on two length scales. Roughness on the nanometer scale appears to be dictated by the size of the crystallites in the film. Roughness on the micron scale is postulated to be related to several factors, including the topography of the SAM and the effects of larger, physisorbed particles or agglomerates. The topographies of the oxide thin films on both the nanometer and micron scales are consistent with a particle-attachment mechanism of film growth.

Order No.: JA906-037

Preparation and ferroelectric properties of mixed composition layered lead zirconate titanate thin films for nonvolatile memory applications

S-H. Kim, D-J. Kim, S.K. Streiffer, A.I. Kingon
(North Carolina University)

Mixed composition layered lead zirconate titanate (PZT) films (Zr/Ti ratio = 30/70 + 65/35) with stoichiometric lead containing PZT thin layer at the film/electrode interface were successfully fabricated by a modified chemical solution deposition method. These modified PZT thin films are highly (111) textured, and have square-shaped P-E hysteresis loops with large remanent polarization and low coercive field, as well as low saturation voltage. In addition, these films show good fatigue and imprint behavior with Pt electrodes; the retained polarization of the modified film was above 50% after fatigue testing to 10^9 cycles, and the thermally induced voltage shifts (ΔV) were 0.51 V after heating at 150 °C for 4410 s, two times lower than for films without a stoichiometric thin layer.

Order No.: JA906-038

Dielectric properties of $Ln(Mg_{1/2}Ti_{1/2})O_3$ as substrates for high-Tc superconductor thin films

S-Y. Cho,[1] C-H. Kim,[1] D-W. Kim,[1] K.S. Hong,[1] J-H. Kim[2]
([1]Seoul National University, [2]Samsung Electro-Mechanics Co., Ltd.)

$Ln(Mg_{1/2}Ti_{1/2})O_3$ (Ln = Dy, La, Nd, Pr, Sm, Y) compositions have been prepared, and their pertinent properties for use as thin film substrates for $YBa_2Cu_3O_x$ (YBCO) were measured. X-ray diffraction shows that $Ln(Mg_{1/2}Ti_{1/2})O_3$ compositions have noncubic symmetry and the $GdFeO_3$-type structure. Dielectric constant measurements revealed values between 22 and 27, which are larger than those of the $LnAlO_3$ family. Quality factor (= 1/tan δ) of the ceramic specimens measured at room temperature were larger than 3000 at 10 GHz. Among the compounds, $La(Mg_{1/2}Ti_{1/2})O_3$ exhibited the highest dielectric constant and the lowest dielectric loss. Chemical reaction was observed between $Ln(Mg_{1/2}Ti_{1/2})O_3$ (Ln = Dy, Sm, Y) and YBCO after annealing at 1 : 1 mixture at 950 °C. Considering dielectric and physical properties, $La(Mg_{1/2}Ti_{1/2})O_3$ and $Sm(Mg_{1/2}Ti_{1/2})O_3$ were determined to be suitable substrates for YBCO thin film used in microwave applications.

Order No.: JA906-039

Possible evidence for the stabilization of β-carbon nitride by high-energy ball milling

Y. Fahmy, T.D. Shen, D.A. Tucker, R.L. Spontak, C.C. Koch
(North Carolina State University)

The possibility of stabilizing the theoretically predicted β–C_3N_4 phase by high-energy ball milling is investigated. Charges of graphitic carbon were milled with and without minor alloying additions under different atmospheric media, namely gas and/or liquid phases of nitrogen, air, or ammonia. Milling was performed at either of two energy levels for periods of up to 48 h. The β–C_3N_4 phase was found to exist as small crystallites in a matrix of primarily amorphous carbon at volume fractions estimated between 5 and 10 at.%. High-resolution electron diffraction and x-ray diffraction indicate that the crystalline nature of the C_3N_4 phase corresponds with a hexagonal lattice with a = 6.46 Å and c/a = 0.374, which are within 2% of the theoretically calculated lattice

parameter values. Analysis of electron energy-loss spectroscopy, x-ray photoelectron spectroscopy, and Fourier transform infrared spectra verify the presence of chemically bonded carbon and nitrogen with chemical states reflecting combined sp^2 and sp^3 hybridization. Chemical analysis confirms nitrogen enrichment at levels consistent with the C_3N_4 stoichiometry and the estimated degree of stabilization. The possible mechanisms responsible for the stabilization of the β–C_3N_4 phase are briefly discussed.
Order No.: JA906-040

Deposition, structure, and hardness of polycrystalline transition-metal nitride superlattice films

X. Chu, M.S. Wong, W.D. Sproul, S.A. Barnett
(Northwestern University)

Polycrystalline TiN/VN, NbN/VN, and TiN/NbN superlattices with periods Λ between 2 and 160 nm were deposited onto steel substrates using an opposed-cathode reactive magnetron sputtering system. The nitrogen partial pressure and the substrate bias values were optimized in order to obtain dense stoichiometric films, which yielded the highest Vickers hardnesses H_v. H_v for TiN/VN and TiN/NbN superlattices reached maximum values of ≈5000 kgf/mm^2 at $\Lambda \approx$ 5–10 nm, compared with ≈2000 kgf/mm^2 for homogeneous TiN, NbN, and VN films. In contrast, $H_v \approx$ 2000 kgf/mm^2 was obtained for VN/NbN superlattices independent of Λ. Model calculations in which the hardness enhancement was proportional to the difference in layer shear moduli gave good agreement with the data. The lack of hardness enhancement in VN/NbN indicates that any other hardening mechanisms, such as coherency strains and dislocation blocking by interfacial misfit dislocations, were not important.
Order No.: JA906-041

Plastic deformation in impure nanocrystalline ceramics

R. Chaim
(Technion—Israel Institute of Technology)

Plastic deformation behavior of impure nanocrystalline ceramics (NCCs) was modeled using the percolative composite model in conjunction with models for plastic deformation by grain boundary sliding. The "glass transition temperature" concept was used to determine the threshold strain rate criterion below which the impure nanocrystalline ceramic would deform plastically. Threshold strain rate is stress-independent. It increases with the temperature increase and with the grain size decrease. Using the dissolution-precipitation model, dependence of the strain rate on temperature, stress, and grain size in the nanometer regime for impure NCCs was calculated. As an example, the critical conditions for plasticity in impure yttria-tetragonal zirconia polycrystals (Y-TZP) were evaluated. At 600 °C, strain rates as high as 10^{-4} s^{-1} were expected in 10 nm impure Y-TZP. Comparison of the published data extrapolated into the nanometer range to the calculated threshold level showed that increase in the applied stress is associated with increase in the grain size and strain rate onsets for plastic deformation.
Order No.: JA906-042

Reactivity in the chromium oxide–calcium fluoride system: An empirical approach

F. Vos, L. Delaey, M. De Bonte, L. Froyen
(Katholieke Universiteit Leuven)

The reaction mechanisms observed when sintering loose Cr_2O_3–CaF_2 powder mixtures were analyzed, and the influence of the sintering parameters on the reaction behavior is presented. Using x-ray diffraction, energy-dispersive spectroscopy, and differential thermal analysis measurements, $CaCrO_4$ was shown to be the reaction product when sintering in air. The reaction occured in two steps. CaF_2 transformed to CaO at the Cr_2O_3–CaF_2 interface, followed by a CaO–Cr_2O_3 interaction, which created the reaction product. Scanning electron microscopy and x-ray fluorescence analysis showed an increasing loss of CaF_2 with increasing sintering temperature and heating rate, while an opposite evolution of the amount of reaction product was observed.
Order No.: JA906-043

Mechanism of in-plane texture development by ion-beam-assisted deposition

H. Ji, G.S. Was
(The University of Michigan)

The objective of this work was to determine the mechanism of in-plane texture development in films made by ion-beam-assisted deposition (IBAD). Both in-plane texture and surface roughness were studied as functions of film thickness. A phenomenological growth model based on the preferential growth of aligned grains due to channeling was proposed, linking the surface roughness evolution and texture development. Good correlation was found between the measured roughness and the model prediction, as well as between the roughness evolution and the in-plane texture development. A critical thickness was introduced at which in-plane texture is completed. Both surface roughness and texture results gave a critical film thickness of 114–250 nm for an ion energy of 1000 eV and R ratio of 0.4. This range of critical film thickness was far beyond the nucleation stage, providing evidence that the development of in-plane texture in IBAD Nb films was growth controlled.
Order No.: JA906-044

Magnetoresistance, temporal evolution, and relaxation of the electrical resistivity in the re-entrant semiconducting $La_{0.80}Ba_{0.20}CoO_3$ perovskite

R.D. Sánchez,[1] J. Mira,[1] J. Rivas,[1] M.P. Breijo,[2] M.A. Señarís-Rodríguez[2]
([1]Universidad de Santiago de Compostela, [2]Universidad de A Coruña)

We report here a study on the electrical and magnetic properties of $La_{1-x}Ba_xCoO_3$ in the re-entrant semiconducting region (x = 0.20). We find that in this material (i) the insulator-metal-insulator sequence is unstable and evolves toward a purely semiconducting behavior—the initial ρ versus T curve can be recuperated upon appropriate annealing treatments; (ii) there are relaxation effects that can be seen by changing the polarity of the electrodes; (iii) there is a negative magnetoresistance $\Delta\rho/\rho$ ~2–3%, for a field as low as 9 kOe, especially at the metal-insulating transition temperatures; and (iv) there are important fluctuations in the electrical resistivity. Taking into account these experimental observations, we can interpret this material as an inhomogeneous system where two thermodynamic phases, one semiconducting and the other metallic and ferromagnetic, coexist although they are crystallographically indistinguishable.
Order No.: JA906-045

Spark plasma sintering of a Nd–Fe–B magnetic alloy

Z.G. Liu,[1] M. Umemoto,[1] S. Hirosawa,[2] H. Kanekiyo[2]
([1]Toyohashi University of Technology, [2]Sumitomo Special Metals Co. Ltd.)

Spark plasma sintering was used to consolidate the crystallized Nd–Fe–B alloy powders. It was found that a higher sintering temperature can improve the consolidation significantly, whereas it deteriorates the magnetic properties drastically due to the appearance of a large amount of α–Fe phase and the grain growth. Sintering at a lower temperature can preserve the magnetic properties better, while the powders cannot be consolidated into a fully dense compact, even under the higher pressure of 75 MPa. Finer starting powder particles show similar behavior.
Order No.: JA906-046

Grain boundary grooving by surface diffusion in $SrTiO_3$ bicrystal

M. Jin. E. Shimada, Y. Ikuma
(Kanagawa Institute of Technology)

A high-purity $SrTiO_3$ bicrystal sample (the angle between two [001] directions is 24°) was used in the present experiment to develop a thermal grain boundary groove along the bicrystal grain boundary at different temperatures (1150–1400 °C) and times (15–6720 min) in air. An atomic force microscope was used to observe the surface morphological change in the annealed bicrystal sample in order to measure the width W and depth h of the developed grain boundary groove. It was found that the log W–log t (at 1150–1400 °C) and the log h–log t (at 1400 °C) relationships are approximately linear, having slopes of approximately 1/4. Using Mullins' formulae, the surface diffusion coefficients of $SrTiO_3$ at different temperatures were calculated. Finally, the surface diffusion coefficient determined in the present experiment appears to correspond to the Titanium atom, which has the lowest diffusivity in $SrTiO_3$.
Order No.: JA906-047

Substrate temperature: A critical parameter for the growth of microcrystalline silicon-carbon alloy thin films at low power

A. Dasgupta,[1] S.C. Saha,[1] S. Ray,[1] R. Carius[2]
([1]Indian Association for the Cultivation of Science, [2]ISI-PV)

P-type microcrystalline silicon-carbon alloy thin films have been prepared at low power by employing the radio-frequency plasma-enhanced chemical vapor deposition technique; judicious choice of deposition parameters is necessary. Substrate temperature has been observed to be the most critical parameter,

while high hydrogen dilution is necessary, but not a sufficient condition for obtaining crystallinity in silicon-carbon alloy thin films. Best microcrystallinity at moderate power density (78 mW/cm^2) has been obtained at a fairly low substrate temperature (180 °C). The highest conductivity of 5.7 Scm^{-1} of a boron-doped microcrystalline sample could be achieved. Incorporation of carbon in these films has been confirmed from x-ray photoelectron spectroscopic studies. However, carbon is incorporated only in the amorphous phase while the crystallites are of silicon only as observed from Raman spectra.
Order No.: JA906-048

Isothermal sections in the Cr–Ga–N system in the 650–1000 °C temperature range

L. Farber, M.W. Barsoum
(Drexel University)

Isothermal sections at 670, 740, and 800 °C in the Cr–Ga–N ternary system were investigated. The presence of the two ternaries, Cr_2GaN and Cr_3GaN, the details of the Cr–Ga and Cr–N binary phase diagrams were confirmed, and the equilibrium diagrams were constructed. At all temperatures, Cr_3GaN was in equilibrium with all the condensed phases, except GaN. In the 670–800 °C temperature range, Cr_2GaN appears to be kinetically stable in contact with GaN. This led to the construction of behavior diagrams that only valid as long as GaN is present in the initial mixture. Above ~910 °C, Cr_2GaN decomposes to form Cr_3GaN, CrN, and Ga(l). At 1000 °C, Cr_3GaN is in equilibrium with all the condensed phases, and CrN is in equilibrium with Ga.
Order No.: JA906-049

An investigation of carbon nanotubes obtained from the decomposition of methane over reduced $Mg_{1-x}M_xAl_2O_4$ spinel catalysts

A. Govindaraj,[1] E. Flahaut,[2] Ch. Laurent,[2] A. Peigney,[2] A. Rousset,[2] C.N.R. Rao[1,3]
([1]Indian Institute of Science, [2]Université Paul-Sabatier, [3]Jawaharlal Nehru Centre for Advanced Scientific Research)

Carbon nanotubes produced by the treatment of $Mg_{1-x}M_xAl_2O_4$ (M = Fe, Co, or Ni, x = 0.1, 0.2, 0.3, or 0.4) spinels with a H_2–CH_4 mixture at 1070 °C have been investigated systematically. The grains of the oxide-metal composite particles are uniformly covered by a weblike network of carbon nanotube bundles, several tens of micrometers long, made up of single-wall nanotubes with a diameter close to 4 nm. Only the smallest metal particles (<5 nm) are involved in the formation of the nanotubes. A macroscopic characterization method involving surface area measurements and chemical analysis has been developed in order to compare the different nanotube specimens. An increase in the transition metal content of the catalyst yields more carbon nanotubes (up to a metal content of 10.0 wt% or x = 0.3), but causes a decrease in carbon quality. The best compromise is to use 6.7 wt% of metal (x = 0.2) in the catalyst. Co gives superior results with respect to both the quantity and quality of the nanotubes. In the case of Fe, the quality is notably hampered by the formation of Fe_3C particles.
Order No.: JA906-050

Microstructural studies by transmission electron microscopy of the formation of ultrathin PtSi layers with novel silicidation processes

S. Jin,[1] H. Bender,[1] R.A. Donaton,[1] K. Maex[1,2]
([1]IMEC, [2]Katholieke Universiteit Leuven)

Ultrathin and uniform Pt-silicide layers are prepared by electron beam evaporation on a heated silicon substrate and by magnetron sputtering at room temperature followed by rapid thermal annealing (RTP) and selective etching, respectively. In the electron-beam deposited samples, continuous Pt-silicide layers of 6–8 nm thickness are formed after thermal annealing. The interfaces between the silicide layers and the silicon substrate are not atomically flat. In the case of the sputtered Pt, continuous PtSi layers down to 3-nm-thick can be produced by using two-step (low-high temperature) and modified two-step (selective etch and high-temperature anneal) RTP silicidation processes. In one-step (high-temperature) processed samples, PtSi is the dominant phase; meanwhile, a small fraction of $Pt_{12}Si_5$ phase is inhomogeneously distributed in the case of thicker PtSi layers. In the two-step RTP-processed samples, a Pt/Pt_2Si/PtSi/Si layered structure is formed after the first RTP step. The first anneal step is found to be crucial for the roughness and epitaxy of the final PtSi layer. The best Schottky barrier heights are found to be 0.249 eV for the 3-nm PtSi/p-Si(100) Schottky diodes. The e-beam and the sputtered PtSi layers follow different epitaxial growth models.
Order No.: JA906-051

Orientation relationship and interfaces in nonfaceted-nonfaceted ZrO_2(c)–$CaZrO_3$ lamellar eutectics

A. Larrea, V.M. Orera, J.I. Peña, R.I. Merino
(Universidad de Zaragoza)

The orientation relationship and the interfaces of ZrO_2(c)–$CaZrO_3$ unidirectional solidified eutectics have been investigated by means of electron diffraction and transmission electron microscopy. In contrast to previous studies on lamellar oxide-oxide systems, neither a constant orientation relationship between contiguous lamellae nor low-index interfaces are observed in this eutectic. As for metals and plastic crystals, it displays incoherent interfaces and nonfaceted growth. This unusual behavior is discussed in terms of entropy of fusion and related to the presence of oxygen vacancies in the ZrO_2(c) phase.
Order No.: JA906-052

A dense transparent ink-jet receptive film that provides instantaneous print drying

B.E. Yoldas
(Carnegie Mellon University)

Ink-jet printing is an important image transfer technology. In this technology, the electronic capabilities are often constrained by shortcomings of materials functions. One of the constraints for fast reproduction of high-resolution photographic quality color images is the print dry time. This presents a challenge in the film technology where large quantities of solvent must be rapidly removed without transporting with colorants outside of the targeted areas. In this work, this is achieved by chemical immobilization of water by organic polymers incorporated into the film matrix. In this dense film, immobilization of large volumes of water becomes possible by a transient local swelling of the matrix—as much as 600–700%. This mechanism of water immobilization not only creates a virtually dry state instantaneously, but also leads to a tighter containment of colorants within the targeted areas, resulting in a significant improvement in edge acuity and image resolution. In addition, the film is printer and ink nonspecific and produces a high gloss on photographic paper.
Order No.: JA906-053

Formation and phase transition of VO_2 precipitates embedded in sapphire

L.A. Gea, J.D. Budai, L.A. Boatner
(Oak Ridge National Laboratory)

Crystallographically coherent precipitates of vanadium dioxide (VO_2) have been formed in the near-surface region of single crystals of sapphire (Al_2O_3) using a combination of ion implantation and thermal treatments. As in the case of either bulk VO_2 single crystals or thin films of VO_2, the thermally induced semiconductor-to-metal phase transition of the embedded VO_2 precipitates is accompanied by a large hysteretic change in the infrared optical transmission. The VO_2 precipitate transition temperature (T_c = 72 to 85 °C) is higher than that of bulk VO_2 (T_c = 68 °C) and is sensitive to the implantation conditions. The present results show that the damage resulting from the co-implantation of vanadium and oxygen into an Al_2O_3 host lattice dictates the final microstructure of the VO_2 precipitates and consequently affects the transition temperature, as well as the optical quality of the VO_2/Al_2O_3 surface-nanocomposite precipitate system.
Order No.: JA906-054

Preparation of non-aggregated Y_2O_3 : Eu phosphor particles by a spray pyrolysis method

Y.C. Kang,[1] S.B. Park,[2] I.W. Lenggoro,[1] K. Okuyama[1]
([1]Hiroshima University, [2]Advanced Institute of Science and Technology)

Y_2O_3 : Eu phosphor particles were directly prepared by a spray pyrolysis method. Photoluminescence, morphology, and crystallinity of the as-prepared particles were investigated. The as-prepared particles above 600 °C had good crystallinity, and the crystallinity increased with increasing reactor temperatures. The particles had spherical morphology and were non-aggregated. The mean size of the particles increased from 0.34 to 1.2 μm when the solution concentration was increased from 0.03 to 1 M. The as-prepared particles had good red emission without annealing at high temperatures when excited with uv light. The main emission peak was 612 nm. The brightness of the as-prepared particles increased with increasing temperatures because of good activation and crystallization at high temperatures.
Order No.: JA906-055

Crystal defects of mordenite structures

S.G. Song
(UOP LLC and United Technologies Research Center)

Crystal defects in mordenite materials were observed and characterized by high-resolution electron microscopy. These defects are identified as line, planar, and 3D defects, which may result in pore blockage of the mordenite channel structure and be detrimental to their chemical properties for catalytic applications. The planar defects are the most severe ones affecting the structural properties of mordenite because of their density and scale. The main emphasis of this investigation is focused on the crystallographic aspects of these defects.

Order No.: JA906-056

The decisive role of oxide content in the formation and crystallization of gallium-lanthanum-sulphide glass

R. Li, D. Furniss, H. Bagshaw, A.B. Seddon
(The University of Sheffield)

A series of gallium-lanthanum-sulphide (GLS) glasses of different oxide concentration has been made, and the spectroscopic properties, thermal properties, and the crystallization behavior of the glasses have been studied. It was revealed that the formability of GLS glasses relies on the existence of a certain amount of oxide content. The thermal stability of GLS glasses changes as a function of oxide concentration. The results have also shown that increasing oxide content caused a shift of the visible absorption edge to shorter wavelengths and an increase of absorption intensity in the infrared region at the multiphonon edge. Two closely related crystalline phases have been identified in the crystallized GLS glasses. For the first time it has been revealed that thermally stable GLS glasses can be made near the eutectic point of these two crystal phases by introducing an optimized amount of oxide.

Order No.: JA906-057

Oxygen and phosphorus coordination around iron in crystalline ferric ferrous pyrophosphate and iron-phosphate glasses with UO_2 or Na_2O

C.H. Booth,[1] P.G. Allen,[1] J.J. Bucher,[1] N.M. Edelstein,[1] D.K. Shuh,[1] G.K. Marasinghe,[2] M. Karabulut,[2] C.S. Ray,[2] D.E. Day[2]
([1]Lawrence Berkeley National Laboratory, [2]University of Missouri)

Fe *K*-edge x-ray absorption fine-structure (XAFS) measurements were performed on glass samples of $(Fe_3O_4)_{0.3}(P_2O_5)_{0.7}$ with various amounts of Na_2O or UO_2. Near-edge and extended-XAFS regions are studied and comparisons are made to several reference compounds. We find that iron in the base glass is ~25% divalent and that the Fe^{2+} coordination is predominantly octahedral, while Fe^{3+} sites are roughly split between tetrahedral and octahedral coordinations. Also, we measure roughly one Fe–O–P link per iron. Substitution of Na_2O or UO_2 up to 15 mol% primarily affects the first Fe–O shell. The results are compared to data from the related material $Fe_3(P_2O_7)_2$.

Order No.: JA906-058

Synthesis and optical characterization of stable and highly luminescent poly-(9-vinylcarbazole)–aluminum-tris-(8-hydroxyquinoline) blends

M. Allegrini, A. Arena, R. Girlanda, C. Pace, S. Patanè, G. Saitta
(Instituto Nazionale per la Fisica della Materia and Università di Messina)

An electrochemical method used to obtain aluminum (III)-8 hydroxyquinoline (Alq_3) blended into poly(N-vinylcarbazole) (PVK) matrix is described. The PVK-Alq_3 blends show an intense green photoluminescence. The intensity increases with the addition of a small percentage of a substituted coumarin to the PVK-Alq_3 solution. The material can be easily spin-coated to obtain homogeneous luminescent thin films suitable for optoelectronic applications. Spectrophotometry in the uv-vis-ir range, photoluminescence, and lifetime measurements are used to characterize the PVK-Alq_3 films.

Order No.: JA906-059

New insights on the crystalline forms in binary systems of n-alkanes: Characterization of the solid ordered phases in the phase diagram tricosane + pentacosane

F. Rajabalee,[1] V. Metivaud,[1] D. Mondieig,[1] Y. Haget,[1] M.A. Cuevas-Diarte[2]
([1]Université Bordeaux, [2]Universitat de Barcelona)

X-ray diffraction analyses of the pure components n-tricosane and n-pentacosane and of their binary mixed samples have enabled us to characterize the crystalline phases observed at "low temperature." On the contrary to what was announced in literature on the structural behavior of mixed samples in odd-odd binary systems with $\Delta n = 2$, the three domains are not all orthorhombic. This work has enabled us to show that two of the domains are, in fact, monoclinic (Aa, Z = 4), and the other one is orthorhombic ($Pca2_1$, Z = 4). The conclusions drawn in this work can be easily transposed to other binary systems of n-alkanes.

Order No.: JA906-060

Hydrothermal growth of hydroxyapatite single crystals under natural convection

K. Teraoka,[1] A. Ito,[2] K. Onuma,[2] T. Tateishi,[2] S. Tsutsumi[3]
([1]National Industrial Research Institute of Nagoya, [2]National Institute for Advanced Interdisciplinary Research, [3]Waseda University)

Whiskerlike-shaped hydroxyapatite single crystals with the calcium-deficient nature were hydrothermally grown under natural convection by using a temperature-gradient-applied pressure vessel. With this method, the crystals grew thinner with a smaller tapering angle than those grown under the nonconvection. Maximum length of the crystals grown under the natural convection was 8.3 mm. The grown crystals survived without fracture through at least ten times maximum indentation (25 μm) of the three-point bending tests, showing the maximum bending angle of 62°. Average tensile strength of the crystals was 410.0 MPa.

Order No.: JA906-061

c-axis lithium niobate thin film growth on silicon using solid-source metalorganic chemical vapor deposition

S.Y. Lee, R.S. Feigelson
(Stanford University)

Textured *c*-axis oriented $LiNbO_3$ films have been grown for waveguiding applications on silicon substrates by the solid-source metalorganic chemical vapor deposition method using tetramethylheptanedionate sources. Thermally grown SiO_2 layers were used as cladding layers to provide optical confinement in the $LiNbO_3$ films. The texture direction could be varied from the [006] to the [012] direction by either increasing the growth temperature and/or decreasing the growth rate. Under optimal growth conditions 100% [006] texturing could be achieved without the aid of an electric field or by using a SiN_x buffer layer. The crystallinity and surface rms roughness of *c*-axis oriented films were found to be strongly dependent on the growth rate. Rocking curve full-width half-maximum values of (006) peaks could be decreased to less than 2° by increasing the growth rate. The surface roughness also decreased with growth rate, and rms values as low as 1.5 nm were achieved. On the other hand, too high a growth rate leads to increased roughness due to gas phase nucleation. The optical losses were closely correlated with surface roughness, and the best films had optical losses near 4.5 dB/cm at a wavelength of 632.8 nm.

Order No.: JA906-062

In situ surface modification and growth of ultra-smooth amorphous carbon films by direct carbon ion-beam deposition

M.H. Sohn, S.I. Kim
(SKION Corporation)

Very thin (<100 nm) amorphous carbon films were grown on silicon substrates by unfiltered and filtered direct carbon ion beams. *In situ* surface modification was performed using C^- energies in the range 300–500 eV prior to the growth of the film. By lowering the energy of the C^- beam to 150 eV, an amorphous carbon film was continuously grown after the surface modification. High-resolution electron microscopy showed that the film/substrate interface was damaged by 400 and 500 eV C^- beams. The carbon composition profile at the interface investigated by electron energy-loss spectroscopy illustrated that the 500 eV C^- beam generated a 30-nm-thick carbon/silicon mixing layer at the interface. The damage and mixing layers were not observed at 300 eV modification. Wear testing found that strong adhesion occurred in samples modified at 400 and 500 eV. However, at 300 eV, modified samples exhibited delamination failure, which indicated inferior adhesion of the films. Surface roughness evolution of 30-, 60-, and 90-nm-thick films was investigated by atomic force microscopy. The film surface roughness decrease as a function of film thickness was much faster when the films were grown by the filtered C^- beam.

Order No.: JA906-063

Microstructural investigation of iron nitride layers formed by low-temperature gaseous nitriding

D.K. Inia,[1] A.M. Vredenberg,[1] D.O. Boerma,[1,2] F.D. Tichelaar,[3] H. Schut,[3] A. van Veen[3]
([1]Utrecht University, [2]Groningen University, [3]Delft University of Technology)

Iron nitride layers were formed by a novel low-temperature gaseous nitriding process. Nitriding occurs at a temperature of 325 °C through NH_3 decomposition at the surface of Ni (25 nm) coated Fe, followed by N transport

through the Ni film into the underlying Fe, where nitride precipitation takes place. The role of Ni is to protect Fe from oxidation by gas impurities and to serve as a catalyst for NH_3 decomposition. The precipitation behavior and the development of microstructure were studied by means of elastic recoil detection, cross-sectional transmission electron diffraction (XTEM), and positron annihilation (PA). From PA and XTEM no evidence was found for the occurrence of porosity during nitriding (an effect found at higher temperatures due to the decomposition of the nitrides into Fe and N_2). XTEM showed that the original columnar α–Fe grains transform into smaller γ'–Fe_4N grains, which subsequently transform into larger ε–$Fe_{3-x}N$ grains. This microstructural evolution of smaller γ' grains forming in the original columnar α–Fe structure occurs in one of two growth modes of the nitride in the Fe layer, i.e., throughout the entire depth range of the Fe layer, or preferentially at the Ni/Fe interface when an iron oxide layer is present at this interface.

Order No.: JA906-064

Hydraulic activity and microstructural characterization of new fly ash-belite cements synthesized at different temperatures

A. Guerrero, S. Goñi, A. Macías, M.P. Luxán
(CSIC)

The influence of the synthesis temperature of a new fly ash-belite cement (FABC) on its hydraulic activity and microstructural characteristics is discussed in this work. Three types of FABC were synthesized at 700, 800, and 900 °C after a previous hydrothermal treatment at 200 °C of the fly ash, CaO, and water mixture. The hydraulic activity of the pastes was evaluated during a period of 200 days from mixing through the combined water content, previously determined from thermogravimetric analyses and the hydration advance degree by x-ray diffraction. The microstructure characterization of the pastes was studied by scanning electron microscopy.

Order No.: JA906-065

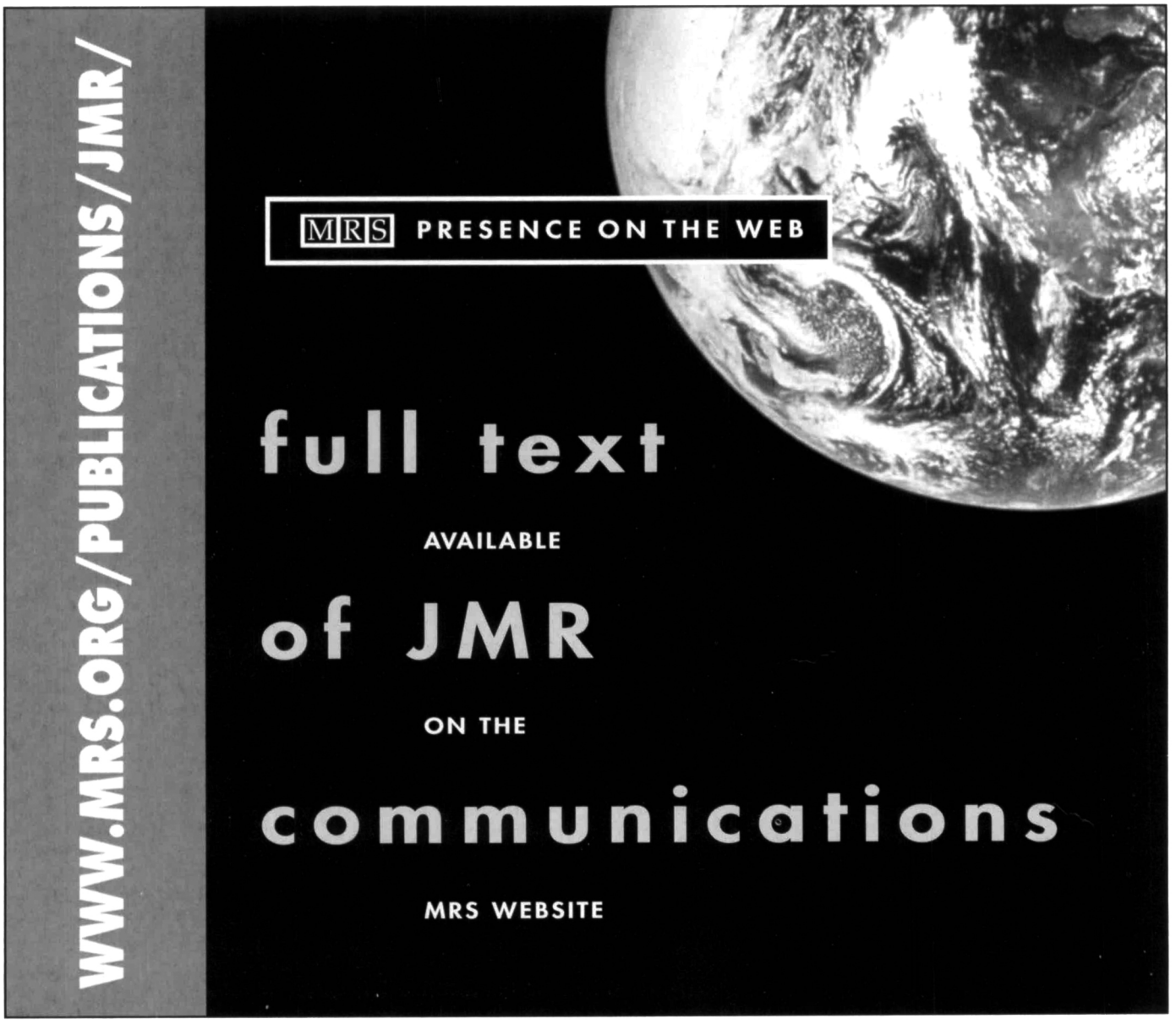

https://doi.org/10.1557/S0883769400052349 Published online by Cambridge University Press